Monthly Notices of the ROYAL ASTRONOMICAL SOCIETY

MNRAS **525,** 527–541 (2023) https://doi.org/10.1093/mnras/stad2181
Advance Access publication 2023 July 21

Towards ultra metal-poor DLAs: linking the chemistry of the most metal-poor DLA to the first stars

Louise Welsh [1,2]★ Ryan Cooke [3] Michele Fumagalli [1,4] and Max Pettini [5]

[1] *Dipartimento di Fisica G. Occhialini, Università degli Studi di Milano Bicocca, Piazza della Scienza 3, I-20126 Milano, Italy*
[2] *INAF – Osservatorio Astronomico di Brera, via Bianchi 46, I-23087 Merate (LC), Italy*
[3] *Centre for Extragalactic Astronomy, Department of Physics, Durham University, South Road, Durham DH1 3LE, UK*
[4] *INAF – Osservatorio Astronomico di Trieste, via G. B. Tiepolo 11, I-34143 Trieste, Italy*
[5] *Institute of Astronomy, University of Cambridge, Madingley Road, Cambridge CB3 0HA, UK*

Accepted 2023 July 7. Received 2023 June 19; in original form 2023 February 7

ABSTRACT

We present new Keck/HIRES data of the most metal-poor damped Ly α (DLA) system currently known. By targeting the strongest accessible Fe II features, we have improved the upper limit of the [Fe/H] abundance determination by $\sim$1 dex, finding [Fe/H] < -3.66 (2σ). We also provide the first upper limit on the relative abundance of an odd-atomic number element for this system [Al/H] < -3.82 (2σ). Our analysis thus confirms that this $z_{\rm abs} \simeq 3.08$ DLA is not only the most metal-poor DLA but also the most iron-poor DLA currently known. We use the chemistry of this DLA, combined with a stochastic chemical enrichment model, to probe its enrichment history. We find that this DLA is best modelled by the yields of an individual Population III progenitor rather than multiple Population III stars. We then draw comparisons with other relic environments and, particularly, the stars within nearby ultra-faint dwarf galaxies. We identify a star within Boötes I, with a similar chemistry to that of the DLA presented here, suggesting that it may have been born in a gas cloud that had similar properties. The extremely metal-poor DLA at redshift $z_{\rm abs} \simeq 3.08$ (i.e. $\sim$2 Gyr after the Big Bang) may reside in one of the least polluted environments in the early Universe.

Key words: stars: population II – stars: population III – galaxies: intergalactic medium – quasars: absorption lines.

1 INTRODUCTION

Tracing chemical evolution from the Cosmic Dawn at $z \sim 15 - 30$ to the present epoch will reveal how the Universe transformed from primordial gas (i.e. primarily hydrogen and helium) to the complex composition of chemical elements we observe locally. Our current understanding suggests that the first generation of stars (known as Population III, or Pop III stars) were the catalysts of this process in the early Universe (see e.g. Bromm & Yoshida 2011). Since the properties of these stars remain elusive to observations, the relative quantities of metals that they produced is also an open question. To understand the earliest epochs of chemical enrichment, we must uncover the properties of the first stars.

Observationally, we have searched for these stars in the local Universe for over four decades (e.g. Bond 1980; Beers, Preston & Shectman 1985; Ryan, Norris & Bessell 1991; Beers, Preston & Shectman 1992; McWilliam et al. 1995; Ryan, Norris & Beers 1996; Cayrel et al. 2004; Beers & Carollo 2008; Christlieb et al. 2008; Roederer et al. 2014; Howes et al. 2016; Starkenburg et al. 2017). None have been found.

Cosmological hydrodynamic simulations that follow the formation of Pop III stars from cosmological initial conditions suggest that the first stars were more massive than the Sun, with typical masses between $10 < {\rm M/M_\odot} < 100$ (Tegmark et al. 1997; Barkana & Loeb 2001; Abel, Bryan & Norman 2002; Bromm, Coppi & Larson 2002; Turk, Abel & O'Shea 2009; Greif et al. 2010; Clark et al. 2011; Hirano et al. 2014; Stacy, Bromm & Lee 2016). If Pop III stars really were limited to these mass scales, their short lifetimes mean they may only be visible at very high redshift; directly observing the supernovae of these stars is one of the flagship goals of the recently launched *JWST*. This facility provides a new avenue to observationally investigate the first stars and galaxies which may revolutionize this field in the coming years (Gardner et al. 2009). A complementary approach to searching for these stars directly is to search for the elements that they produced.

Reservoirs of gas, detected as absorption along the line-of-sight towards unrelated background quasars, are reliable probes of cosmic chemical evolution. These low density structures allow us to trace the evolution of metals from $0 < z < 5$ with a consistent degree of sensitivity (Péroux & Howk 2020). The absorption line systems whose column density of neutral hydrogen exceeds $\log_{10}(N({\rm H\,I})/{\rm cm}^{-2}) \geq 20.3$ are known as Damped Ly α systems (DLAs; see Wolfe, Gawiser & Prochaska 2005 for a review). DLAs are uniquely suited to high-precision chemical abundance studies; the large column density of neutral hydrogen means that the gas is optically thick to ionizing radiation and the constituent metals reside primarily in a single, dominant ionization state. This negates the need for ionization corrections and, thus, the column density of the observed ionic species can be used to accurately determine the relative metal abundances of the gas reservoir. These objects

★ E-mail: louise.welsh@unimib.it

are most easily studied in the redshift interval $2 < z < 3$, when the rest-frame UV lines (e.g. H I λ1215 and Fe II λ2382) are shifted into the optical wavelength range. However, DLAs can be studied at any redshift once an appropriate sightline (e.g. a quasar) has been identified.

Studies which probe $z > 6$ sightlines trace the composition of gas closer to the epoch of the Cosmic Dawn (Becker et al. 2011, 2019; Bosman et al. 2022; D'Odorico et al. 2022, 2023). However, at these redshifts, it can be challenging to observe the characteristic Ly α absorption, which is required to determine the metallicity. The column density of neutral hydrogen can only be determined for proximate systems which are less frequent and suffer additional challenges due to the proximity to the background quasar (Simcoe et al. 2012; Bañados et al. 2019). It may be that the systems found at lower redshift offer the best opportunity to identify relic metals with high-precision.

Indeed, there may be some near-pristine gaseous reservoirs in the early Universe that have been solely enriched by the supernovae (SNe) of the first stars (Erni et al. 2006; Pettini et al. 2008; Cooke, Pettini & Steidel 2017; Welsh, Cooke & Fumagalli 2019; Nuñez, Kirby & Steidel 2022). The metallicity of these reservoirs provides an indication of the level of enrichment the gas has experienced from stellar populations. In principle, this property is easily defined as the amount of metals in the system relative to the hydrogen content. This is often expressed as [X/H].[1] However, the metal (or combination of metals) used in this expression is dependent on the system being analysed and, ultimately, on the accessible features.

A typical metallicity tracer is often [Fe/H] (i.e. the relative abundance of iron to hydrogen – which we call the Fe-metallicity); anything that is 1000 times more Fe-poor than the Sun (i.e. [Fe/H] < -3) is considered extremely metal-poor (EMP), while an environment that is 10 000 times more Fe-poor than the Sun (i.e. [Fe/H] < -4) is considered ultra metal-poor (UMP) (see Beers & Christlieb 2005, for the definitions used to describe different levels of metal-paucity). As we continue to discover increasingly Fe-poor objects, peculiar chemical abundance patterns become more apparent. The lowest Fe-metallicity environments are often associated with enhanced abundances of α-elements. This is well-documented through the analysis of metal-poor Milky Way halo stars (i.e. the stellar relics) where a deficit of Fe is frequently identified alongside an overabundance of C. These stars are known as carbon-enhanced metal-poor stars (i.e. CEMP stars; see Beers & Christlieb 2005). There have been reports of a similar carbon-enhancement in both metal-poor DLAs (Cooke et al. 2011a) and lower column density gas reservoirs (i.e. Lyman limit systems; LLSs – see Zou et al. 2020; Saccardi et al. 2023). Though, an updated analysis of the C-enhanced DLA revealed a [C/Fe] abundance ratio that is only modestly enhanced relative to the metal-poor DLA population (Dutta et al. 2014; Welsh et al. 2020). Generally, we note that, when α-elements are detected in excess alongside a minimal contribution from Fe, metallicity estimates based on Fe fail to describe the overall metal-paucity of the system in question. This is worth considering when we are searching for chemically near-pristine gas.

We are yet to detect a chemically pristine DLA, although there are multiple LLSs that appear to be entirely untouched by the process of star formation (e.g. Fumagalli, O'Meara & Prochaska 2011; Robert et al. 2019). There is the potential detection of an UMP DLA at $z \sim 7$ (Simcoe et al. 2012), but this hinges on the modelling of the quasar emission (see Bosman & Becker 2015, for an alternative interpretation of these data). Hence, we are also yet to firmly detect an UMP DLA. Prior to the collection of the data presented here, there have been three high-precision detections of EMP DLAs with associated iron abundance errors < 0.20 dex (Ellison et al. 2010; Cooke et al. 2011b, 2016; Welsh et al. 2022). Rafelski et al. (2012) report a metallicity floor across a statistical sample of DLAs that is [M/H] $\simeq -3$. Thus, the detection of an UMP DLA would mark an exceptional environment. Future surveys like WEAVE, DESI, and 4MOST will provide much improved statistics, necessary to reveal where UMP DLAs lie within the population of known absorbers (Dalton et al. 2012; de Jong et al. 2012; DESI Collaboration 2016; Pieri et al. 2016).

The DLA found towards the quasar SDSS J090333.55+262836.30 (hereafter J0903+2628) is the *most* metal-poor DLA currently known (Cooke et al. 2017). This was determined through the analysis of absorption from low ionic species such as C II, O I, and Si II. The strongest Fe II feature available with those data was the weak Fe II λ1260 transition; in order to observe the absorption due to the lighter atomic number elements together with the associated H I, Cooke et al. (2017) adopted an instrument setup that did not cover several stronger Fe II transitions. As a result, the data presented in Cooke et al. (2017) only provided a relatively weak upper limit on the iron abundance, [Fe/H] < -2.81 (2σ). Given the extreme paucity of both α-elements and Fe observed for this system, we have sought additional high resolution observations that target the stronger Fe II λ1608 and Fe II λ2382 features. These observations also target the Al II λ1670 feature – providing the first insight into the abundance of an odd atomic number element for this DLA. In this paper, we utilize these additional data to reevaluate the most likely enrichment scenario of this DLA. We also present the first stochastic chemical enrichment analysis of this near-pristine gas cloud, and test if this environment might have been enriched by the first generation of stars.

This paper is organized as follows. Section 2 describes our observations and data reduction. We present our data in Section 3 and investigate the chemical enrichment history of this system in Section 4. In Section 5, we present our discussion and draw comparisons with other relic environments, before drawing overall conclusions and suggesting future work in Section 6.

2 OBSERVATIONS AND DATA REDUCTION

The DLA towards the $m_r = 19.0$ quasar J0903+2628 (SDSS J090333.55+262836.30), at $z_{em} = 3.22$ has previously been identified as the most metal-poor DLA currently known. We have acquired an additional 9 h of echelle spectroscopic data on the associated quasar using the High Resolution Echelle Spectrometer (HIRES; Vogt et al. 1994) mounted on the 10 m Keck I telescope. These data were collected through 9×3600 s exposures across two half nights between 2021 December 18 - 27. We utilize the red cross-disperser to target the strongest available Fe II features that fall at red wavelengths. The data cover $5450 - 10\,000$ Å with small wavelength gaps due to both the detector mosaic and the configuration of the instrument (that results in incomplete coverage across a small number of the reddest echelle orders). We use the C1 decker resulting in a slitwidth =0.861 arcsec and a nominal resolution of $R = 49\,000$ corresponding to a velocity full-width at half-maximum $v_{FWHM} = 6.28$ km s^{-1}.

[1]This denotes the logarithmic number abundance ratio of elements X and H relative to their solar values $X_\odot$ and $H_\odot$, i.e. [X/H] $= \log_{10}(N_X/N_H) - \log_{10}(N_X/N_H)_\odot$.

The collected data were binned 2 × 2 during readout. These HIRES data were reduced with the Hires REDUX[2] reduction pipeline (Bernstein, Burles & Prochaska 2015). This pipeline includes the standard reduction steps of subtracting the detector bias, locating and tracing the echelle orders, flat-fielding, sky subtraction, optimally extracting the 1D spectrum, and performing a wavelength calibration. The data were converted to a vacuum and heliocentric reference frame.

Finally, we combined the individual exposures of this DLA using UVES_POPLER.[3]This corrects for the blaze profile, and allowed us to manually mask cosmic rays and minor defects from the combined spectrum. When combining these data we adopt a pixel sampling of 2.5 km s^{-1}.

These new data are analysed in the following section in combination with the original HIRES data collected in 2016 (presented in Cooke et al. 2017). These data were collected using an identical instrument setup barring the wavelength coverage, which instead spanned 3700–6530 Å. The original observations were executed as 9 × 3600 s exposures (resulting in a combined time on source across both programmes of 18 h). For further details, we refer the reader to the original paper. Given both spectra, we cover the optimal features necessary to conduct a detailed investigation of the chemistry of the DLA towards J0903+2628.

3 ANALYSIS

Using the Absorption LIne Software (ALIS) package[4] – which uses a χ-squared minimization procedure to find the model parameters that best describe the input data – we simultaneously analyse the full complement of high S/N and high spectral resolution data currently available for the DLA towards J0903+2628. We model the absorption lines with a Voigt profile, which consists of three free parameters: a column density, a redshift, and a line broadening. We assume that all lines of comparable ionization level have the same redshift, and any absorption lines that are produced by the same ion all have the same column density and total broadening. The total broadening of the lines includes a contribution from both turbulent and thermal broadening. The turbulent broadening is assumed to be the same for all absorption features, while the thermal broadening depends inversely on the square root of the ion mass; thus, heavy elements (e.g. Fe) will exhibit absorption profiles that are intrinsically narrower than the profiles of lighter elements (e.g. C). The intrinsic model is then convolved with the line spread function of the instrument; this results in an additional apparent broadening of the lines. We note that we simultaneously fit the absorption and quasar continuum. We model the continuum around every absorption line as a low-order Legendre polynomial (typically of the order of 3). We assume that the zero-levels of the sky-subtracted HIRES data do not depart from zero.[5] Finally, we introduce one additional free parameter that accounts for a relative velocity shift in the wavelength solution between the two epochs. The best-fitting value ($\Delta v = 4 \pm 2$ km s^{-1}) is driven by Si II λ1526, which is the only transition in common between the two data sets.

The DLA towards J0903+2628 is best modelled by three absorption components for C II and Si II at redshifts $z_{\rm abs} = 3.077590 \pm 0.000002$, $z_{\rm abs} = 3.076653 \pm 0.000005$, and $z_{\rm abs} = 3.076331 \pm 0.000006$. The O I and Fe II features are best modelled by the two highest redshift components only. We attempted to model the intrinsically weak Al II feature solely using the highest redshift component; we instead report an upper limit. Due to the blending between the components, we cannot directly determine the temperature of the gas reservoir. We therefore assume $T = 1 \times 10^4$ K (this is typical for metal-poor DLAs; see Cooke, Pettini & Jorgenson 2015; Welsh et al. 2020; Noterdaeme et al. 2021). Given this assumed temperature, the associated turbulent broadening of these components are best described by the Doppler parameters $b_1 = 8.8 \pm 0.3$ km s^{-1}, $b_2 = 9.6 \pm 0.5$ km s^{-1}, and $b_3 = 14.9 \pm 0.7$ km s^{-1}, respectively. The data, along with the best fitting model, are shown in Fig. 1 while the resulting column densities and relative abundances are presented in Table 1. We note that, when modelling the data, we allow the relative abundances of metals to vary from component to component. We have repeated our analysis under the assumption that the relative abundances of metals (i.e. the [O/Fe] ratio) must be the same in all components; the resulting total abundances are consistent with those reported in Table 1. Without this assumption, the third components at $z_{\rm abs} = 3.076331$ (i.e. the bluest component) indicates an unusually high Si II/C II ratio. This could be due to several possibilities: (1) an unfortunate blend near Si II λ1260 (at $v \simeq -90$km s^{-1} in Fig. 1), that masquerades as Si II absorption; (2) ionization effects; or (3) a peculiar enrichment source. The reality of this Si II absorption can be tested with deeper data of the other strong Si II absorption lines (e.g. this feature may not be detected in Si II λ1526, but the data are of too low S/N to be confident at this stage). The composition of this third component has a negligible impact on our subsequent analysis; we consider only the chemistry of the predominantly neutral components (i.e. those traced by O I). We have also repeated our analysis assuming a temperature range of (0.5–2.0) × 10^4 K and found that the abundances in Table 1 are stable against these changes. This is not surprising, since all of the detected absorption lines are weak enough to be in the linear regime of the curve of growth, and are therefore relatively insensitive to the relative amounts of Doppler, thermal, and instrumental broadening. In this metallicity regime, we do not expect our observed abundances to be impacted by any appreciable dust depletion (Pettini et al. 1997; Akerman et al. 2005; Vladilo et al. 2011; Rafelski et al. 2014).

The reported relative abundances are consistent with those found using the original HIRES data. Notably, we have improved the upper limit on the [Fe/H] abundance determination by $\sim$ 1 dex from [Fe/H] < -2.81 (2σ) to [Fe/H] ≤ -3.66 (2σ). The DLA in question is therefore pushing towards the UMP regime at [Fe/H] < -4. We also place the first upper limit on the abundance of an odd-atomic number element, [Al/H] ≤ -3.82 (2σ), of this EMP gas cloud.

We note that the data near the Fe II λ2382 feature is relatively noisy compared to the data near features at bluer wavelengths. This is, in part, due to the challenges associated with observing faint targets near 9700 Å (where this feature falls) from the ground. We have checked for possible blending with known telluric absorption and found nothing significant. This feature is the strongest Fe II line (i.e. has the largest oscillator strength) covered by our spectrum. Though we do not cover the Fe II λ2344 feature, we do additionally observe Fe II λ1260 and Fe II λ1608. These lines are relatively weaker, however, they fall in regions of the spectrum that are not influenced by telluric lines. The combined information provided by these Fe II features are essential to investigate the Fe content of this DLA.

[2]Hires REDUX is available from: https://www.ucolick.org/~xavier/HIRedux/

[3]UVES_POPLER is available from: https://github.com/MTMurphy77/UVES_popler

[4]ALIS is available from: https://github.com/rcooke-ast/ALIS.

[5]We visually inspected the troughs of saturated absorption features to confirm this is the case.

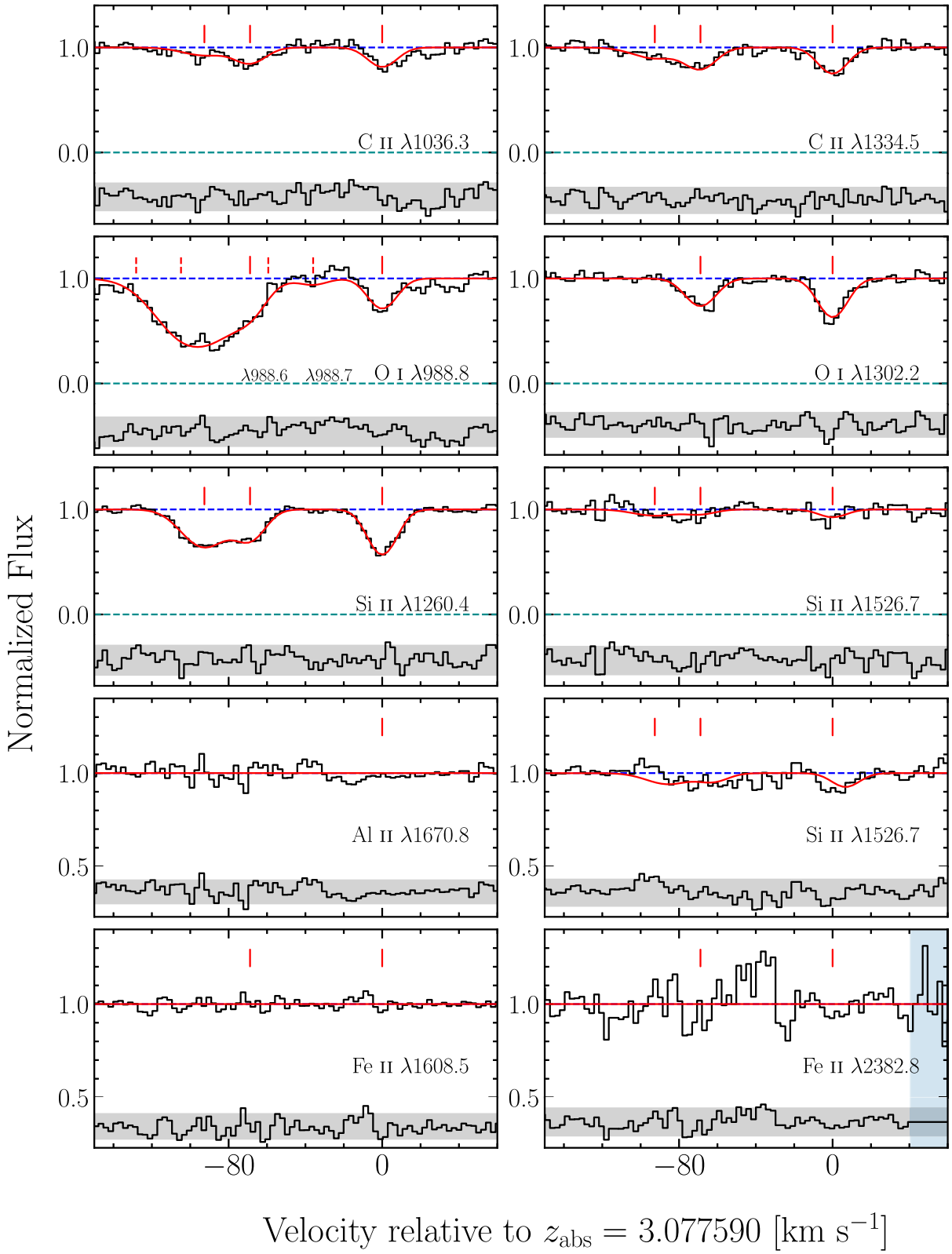

Figure 1. Continuum normalized HIRES data (black histograms) of the absorption features produced by metal ions associated with the DLA at $z_{\rm abs} = 3.077590$ towards the quasar J0903+2628. The best-fitting model is shown with the red curves. The blue dashed line indicates the position of the continuum while the green dashed line indicates the zero-level. Note the different scale of the y-axes of the bottom two rows. These bottom two rows correspond to the data collected in 2021 while the upper three rows correspond to the 2016 Keck/HIRES data. The red ticks above the absorption features indicate the centre of the Voigt line profiles for each identified component. The dashed-red lines in the third panel highlight the components of the O I λ988 triplet. Note that the deep broadening seen at <-50 km s^{-1} in the O I 988 panel is due to unrelated blending. Below the zero-level, we show the residuals of this fit (black histogram) where the grey shaded band encompasses the 2σ deviates between the model and the data. The blue-shaded regions encompass data excluded from the fit.

Table 1. Ion column densities of the DLA at $z_{\rm abs} = 3.077590$ towards the quasar J0903+2628. The quoted column density errors are the 1σ confidence limits while the column densities are given by $\log_{10} N({\rm X})/{\rm cm}^{-2}$.

Ion	Transitions used (Å)	Solar*	Comp. 1 $z_{\rm abs} = 3.077590$	Comp. 2 $z_{\rm abs} = 3.076653$	Comp. 3 $z_{\rm abs} = 3.076331$	Total	[X/H]	[X/Fe]
H I	1215	12.00	–	–	–	20.32 ± 0.05	–	–
C II	1036, 1334	8.43	13.07 ± 0.03	12.99 ± 0.04	12.83 ± 0.06	13.33 ± 0.02	-3.42 ± 0.06	$>+0.24$
O I	988, 1302	8.69	13.70 ± 0.02	13.55 ± 0.03	–	13.93 ± 0.02	-3.08 ± 0.05	$>+0.58$
Al II	1670	6.45	≤ 10.95[a]	–	–	≤ 10.95[a]	≤ -3.82[a]	–
Si II	1260, 1526	7.51	12.40 ± 0.01	12.20 ± 0.03	12.50 ± 0.02	12.61 ± 0.01	-3.22 ± 0.05	$>+0.44$
Fe II	1260, 1608, 2382	7.47	≤ 11.83[a]	≤ 11.83[a]	–	≤ 12.13[a]	≤ -3.66[a]	–

Notes. *We adopt the solar abundances reported in Asplund et al. (2009). These are consistent with those recommended by Lodders (2019) when considering the associated uncertainties. The total column densities and abundance ratios are based on the chemistry of the predominantly neutral components (i.e. Comp 1 and 2).
[a]2σ upper limit on column density.

These new data reaffirm that the DLA towards J0903+2628 is the most metal-poor DLA currently known. It has the lowest C, O, Si, and Fe abundance determination of any known DLA. We also searched for absorption from higher ion stages, such as Si III, so that we can determine the ionization ratio and subsequently model the density of the gas reservoir. However, the strong Si III λ1206 feature is heavily blended with unrelated absorption. In the following sections, we investigate the chemical enrichment history of this DLA using our stochastic chemical enrichment model and the yields from simulations of Population III SNe.

4 CHEMICAL MODELLING

4.1 Chemical enrichment model

Using the observed abundance pattern of this DLA, alongside the stochastic chemical enrichment model described in Welsh et al. (2019), we investigate the possible enrichment history of this DLA. The basis of our model is described briefly below. The singular update since previous applications is the treatment of upper limits. When accounting for the error associated with the observed data we take two approaches. For abundances with known errors, this distribution is modelled with a Gaussian distribution function. For abundances with upper limits, this distribution is modelled by a Q-function.

4.1.1 Likelihood modelling technique

The mass distribution of Population III stars is modelled as a power law: $\xi(M) = k\,M^{-\alpha}$, where α is the power-law slope,[6] and k is a multiplicative constant that is set by defining the number of stars, $N_\star$, that form between a minimum mass $M_{\rm min}$ and maximum mass $M_{\rm max}$, given by:

$$N_\star = \int_{M_{\rm min}}^{M_{\rm max}} k M^{-\alpha} {\rm d}M \ . \quad (1)$$

In this work, $N_\star$ represents the number of stars that have contributed to the enrichment of a system. Since the first stars are thought to form in small multiples, this underlying mass distribution is necessarily stochastically sampled. We utilize the yields from simulations of stellar evolution to construct the expected distribution of chemical abundances given an underlying IMF model. These distributions can then be used to assess the likelihood of the observed DLA abundances given an enrichment model.

[6]In our formulation, $\alpha = 2.35$ corresponds to a Salpeter IMF.

We utilize the yields from Heger & Woosley (2010) (hereafter HW10) to construct the expected distribution of chemical abundances given an underlying IMF model. The HW10 simulations trace nucleosynthesis processes within Population III progenitors across their lifetimes and calculate the ejected yields of elements following the eventual collapse of these stars as core-collapse SNe (CCSNe). These simulations explore initial progenitor masses in the range $M =$ (10–100) $\rm M_\odot$, explosion energies from $E_{\rm exp} = (0.3\text{–}10) \times 10^{51}$ erg, and mixing parameters from $f_{\rm He} = 0\text{–}0.25$. The explosion energy is a measure of the final kinetic energy of the ejecta at infinity, while the mixing between stellar layers is parametrized as a fraction of the helium core size. This parameter space is evaluated across 120 masses, 10 explosion energies, and 14 mixing parameters. We linearly interpolate between this grid of yields during our analysis. We refer the reader to HW10 and Welsh et al. (2019) for further details and caveats related to these yield calculations.

Our model contains six parameters: $N_\star$, α, $M_{\rm min}$, $M_{\rm max}$, $E_{\rm exp}$, and $f_{\rm He}$. The range of model parameters we consider are:

$$\begin{aligned} -5 \leq \quad & \alpha & \leq 5 \ , \\ 1 \leq \quad & N_\star & \leq 150 \ , \\ 0.3 \leq \quad & E_{\rm exp}/10^{51}{\rm erg} & \leq 10 \ , \\ 12 \leq \quad & M_{\rm max}/{\rm M}_\odot & \leq 70 \ . \end{aligned}$$

In what follows, we assume that stars with masses >10 $\rm M_\odot$ are physically capable of undergoing core collapse. Therefore, we fix $M_{\rm min} = 10$ $\rm M_\odot$. We also assume that the mixing during the explosive burning phase of the SN occurs within a region 10 per cent of the helium core size (i.e. $f_{\rm He} = 0.100$). This is the fiducial choice from HW10 based on their comparison with the Cayrel et al. (2004) stellar sample. These empirically motivated constraints reduce the number of free parameters to 4. This ensures the remaining model parameters can be optimally estimated based on the number of currently known abundance ratios. We apply uniform priors to all remaining model parameters. Note that the upper bound on $M_{\rm max}$ corresponds to the mass limit above which pulsational pair-instability SNe are believed to occur (Woosley 2017). We allow $M_{\rm max}$ to be a free parameter to account for any 'islands of explodability' that could influence the collapse of these progenitors; simulations from Sukhbold, Woosley & Heger (2018) find that there may be a mass above which the entire star collapses directly to a black hole. Given this possibility, our model utilizes the assumption that stars born with a mass above $M_{\rm max}$ will collapse directly to black holes without any chemical yield.

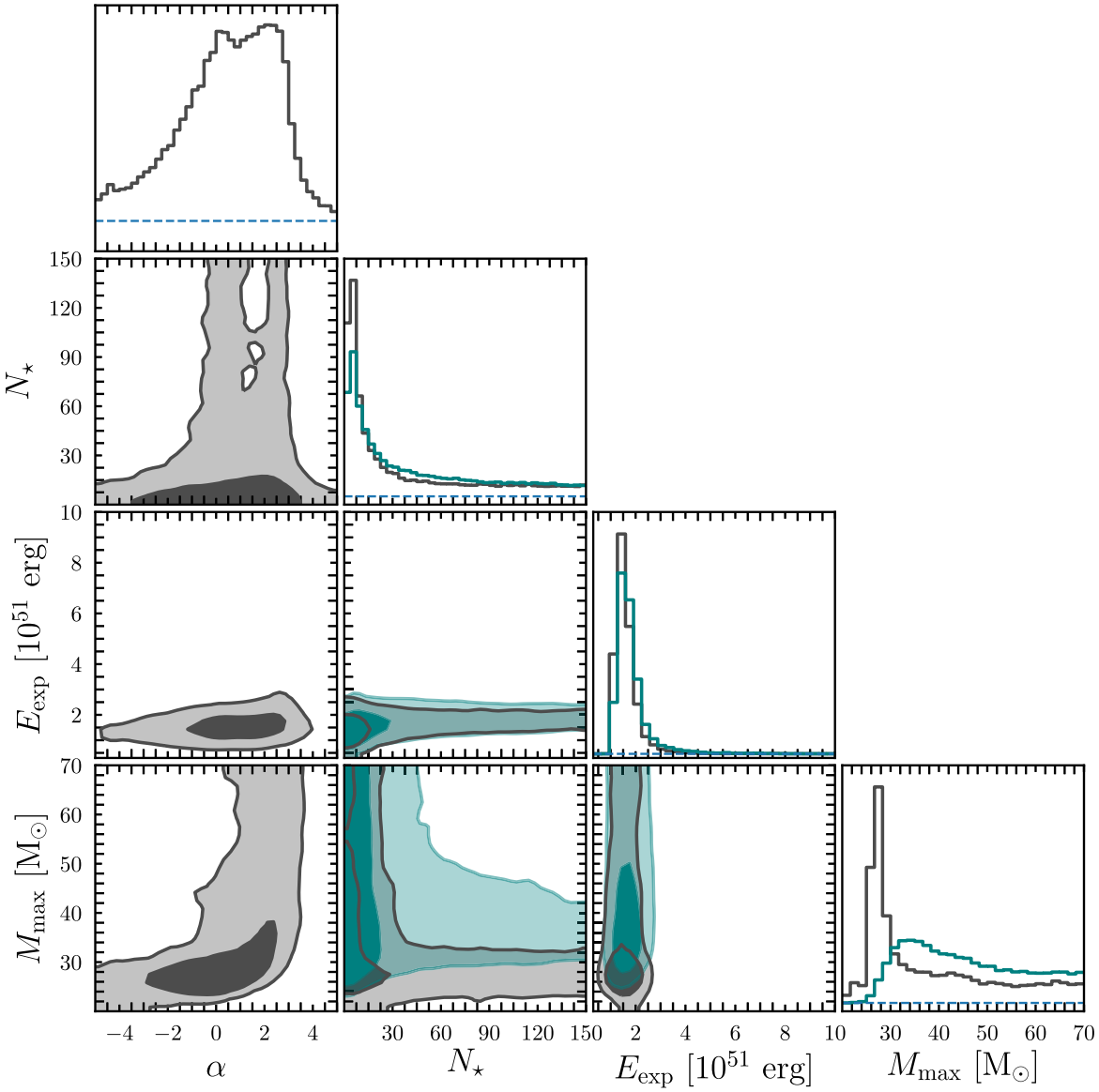

Figure 2. The marginalized maximum likelihood distributions of our fiducial model parameters (main diagonal), and their associated 2D projections, given the known chemistry of the DLA towards J0903+2628. The dark and light contours show the 68 per cent and 95 per cent confidence regions of these projections, respectively. The horizontal blue dashed lines mark where the individual parameter likelihood distributions fall to zero. The grey distributions correspond to the analysis of the full parameter space, described in Section 4.1. The green distributions are the result of imposing a Salpeter slope for the IMF (i.e. $\alpha = 2.35$).

4.2 Application to DLA data

Using all available chemical abundance measurements of the DLA towards J0903+2628 we run a Markov Chain Monte Carlo (MCMC) maximum likelihood analysis to find the enrichment model that best fits these data. The converged chains are shown in Fig. 2 for both a Salpeter IMF (green histograms and contours) and a power-law IMF where the slope is a free parameter (grey histograms and contours). The inferred enrichment models are broadly consistent for both the choice of a varying and fixed IMF slope. This is to be expected since the maximum likelihood estimate of α for the varying IMF slope is consistent with that of a Salpeter distribution at the 95 per cent confidence level. However, we note there is preference towards a flat or even top-heavy IMF slope. The inferred number of enriching stars shows a preference towards low values of $N_\star$. The distribution of the typical explosion energy is more clearly centred around $E_{\rm exp} \sim 1.8 \times 10^{51}$ erg. Both the distribution of $N_\star$ and $E_{\rm exp}$ are stable against changes to the slope of the IMF. In contrast to this, the inferred maximum mass of the enriching star is dependent on the slope of the IMF. For a Salpeter distribution, there is a preference towards $M_{\rm max} > 40$ M$_\odot$; this can be seen from the plateau in the distribution shown by the green curve in the bottom right-hand panel of Fig. 2. For the case of a varying IMF slope, there is a peak in the distribution of the maximum mass at $M_{\rm max} \sim 25$ M$_\odot$. This is driven by the possibility of both flat and top-heavy IMFs. This can be seen by the correlation between α and $M_{\rm max}$ in the bottom left-hand panel of Fig. 2. These results are consistent with our previous investigations of the enrichment of metal-poor DLAs.

The broad distributions in Fig. 2 highlight the lack of preference towards a particular enrichment model (e.g. both the number of enriching stars and the maximum stellar mass are relatively unconstrained). To investigate the origin of this, we test how well the

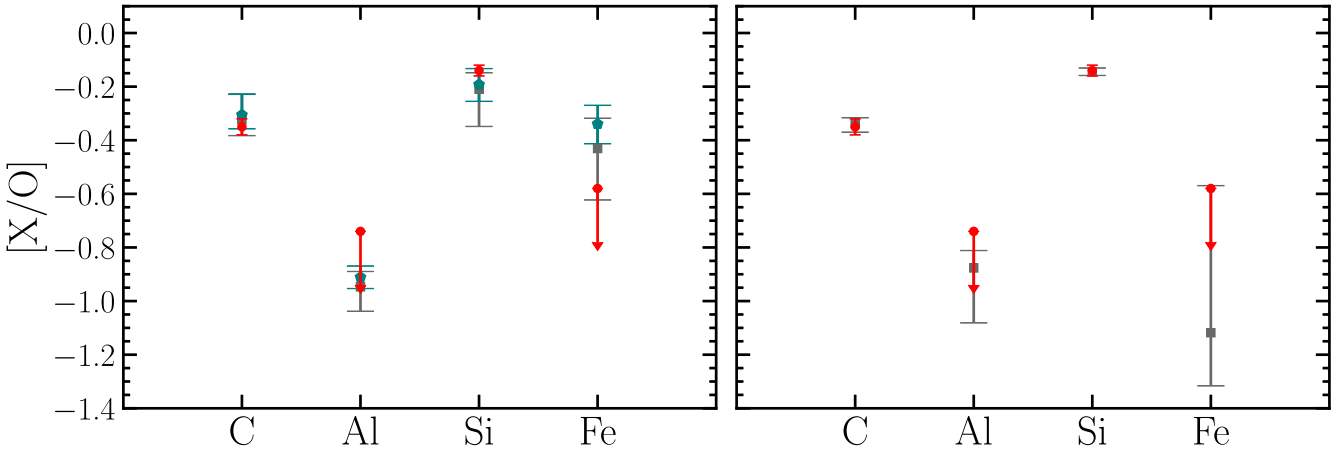

Figure 3. Left-hand panel: Modelled abundances (grey) versus observed data (red) given a stochastic enrichment model with a free IMF slope. The model successfully reproduces all chemical abundance measurements. The grey data show the median predicted value and the interquartile range of predicted abundances given the data. The modelled abundances given a Salpeter IMF are shown in green. Right-hand panel: Modelled abundances (grey) versus observed data (red) under the assumption that the environment has been enriched by 1 Population III SN.

inferred model can replicate the data. Using our stochastic enrichment model, we can recover the predicted abundance pattern given the inferred parameter distributions. Fig. 3 (left-hand panel) shows the observed abundances (red symbols) alongside the modelled abundances for the case of a free IMF slope (grey symbols) and for a Salpeter IMF (green symbols). While the observed abundance pattern is well-recovered, there is a preference towards a top-heavy IMF and a low number of enriching stars. The predicted abundances given a Salpeter IMF do not produce the same agreement with the observed abundances of the DLA. This is primarily driven by the predicted [Fe/O] abundance given a Salpeter IMF. The remaining relative abundances are predicted equally well by both scenarios. This highlights both the importance of considering multiple relative abundances simultaneously and the sensitive nature of abundance pattern fitting. We note that, given the current associated errors, there would be little distinction between the performance of either model at the 3σ level of confidence. This is further motivation to obtain high-precision abundance determinations for these rare gaseous relics. Since these data are best modelled by a low number of enriching stars, we will now consider the possibility that this system has been enriched by a single Population III SN. This idea was previously considered by Cooke et al. (2017), and we now reevaluate the best-fitting model parameters given the new abundance information.

4.2.1 *Enrichment by one Pop III SN*

The results of considering a single Pop III progenitor are shown in Fig. 4 (and the right-hand panel of Fig. 3). Note that, in this scenario, we allow the degree of mixing to vary as a free parameter with a uniform prior. Fig. 4 highlights that there is a bimodal distribution of the inferred initial progenitor mass, concentrated in the mass range $M = (18\text{–}27)\ \mathrm{M}_{\odot}$. The corresponding explosion energy of this progenitor is in the range $E_{\rm exp} = (0.6\text{–}1.8) \times 10^{51}$ erg (1σ) and there is preference towards a low degree of mixing between the stellar layers, $f_{\rm He} < 0.1$ (1σ), though it is unconstrained at the 2σ level. The lack of information regarding the degree of mixing is curious. To investigate this further, we have explored the combination of progenitor parameters best able to individually fit the data. We isolate these models based on their log-likelihood value. Fig. 5 shows a subset of these progenitor models and the associated predicted abundances. Specifically, we display the 10 progenitor models with the largest log-likelihood values. We find that these models are almost identical barring the degree of mixing. Notably, these model span a large fraction of the $f_{\rm He}$ parameter space and are a driving force behind the large spread of the predicted [Fe/O] abundance shown in the right-hand panel of Fig. 3. We therefore expect that the mixing parameter can be pinned down once the Fe II column density of this system is confidently measured. In Appendix A, we compare these model distributions to those originally inferred in Cooke et al. (2017). In summary, we find that the latest limits on [Fe/O] and [Al/O] are sufficiently informative to rule out the previously inferred enrichment scenario.

In Fig. 3 (right panel), we show the modelled abundance ratios given the distributions of progenitor parameters shown in Fig. 4. Through the comparison of the left and right hand panels of this figure, it is clear that the scenario of enrichment by an individual Population III SN is a similarly good fit to the data as the fiducial stochastic model. The predicted abundances in both scenarios are likely being drawn from similar progenitors. The maximum likelihood parameter estimates from the stochastic model are consistent with sampling an individual $\sim$25 $\mathrm{M}_{\odot}$ progenitor (achieved via a top-heavy IMF model with $N_{\star} = 1$ and $M_{\rm max} = 25\ \mathrm{M}_{\odot}$). To further compare the relative performance of these models we consider the Akaike Information Criterion (AIC) (Akaike 1974). The AIC is given by $\mathrm{AIC} = 2K - 2\ln(\mathcal{L})$ where K is an indication of the number of free parameters[7] and $\mathcal{L}$ is the maximum likelihood of the model. The AIC given the stochastic model is 14. For the individual Pop III progenitor model the $AIC = 3$; this relatively lower value indicates that modelling the enrichment via one Pop III SN is better able to reproduce these data. We also note that the observed upper limit of [Fe/O] is more easily explained given the yields of an individual Population III SN. Though, the true level of agreement is reserved for definitive [Fe/O] and [Al/O] measurements. Indeed it is possible that with future data, and an increasingly extensive abundance pattern determination, our current model may be ruled out. At present, it is interesting that the known abundances of this DLA are preferably

[7]Specifically, $K = 2 + n$, where n is the number of free model parameters. In the case of the stochastic model with a free IMF slope, $n = 4$. For the case of an individual Pop III enricher $n = 3$.

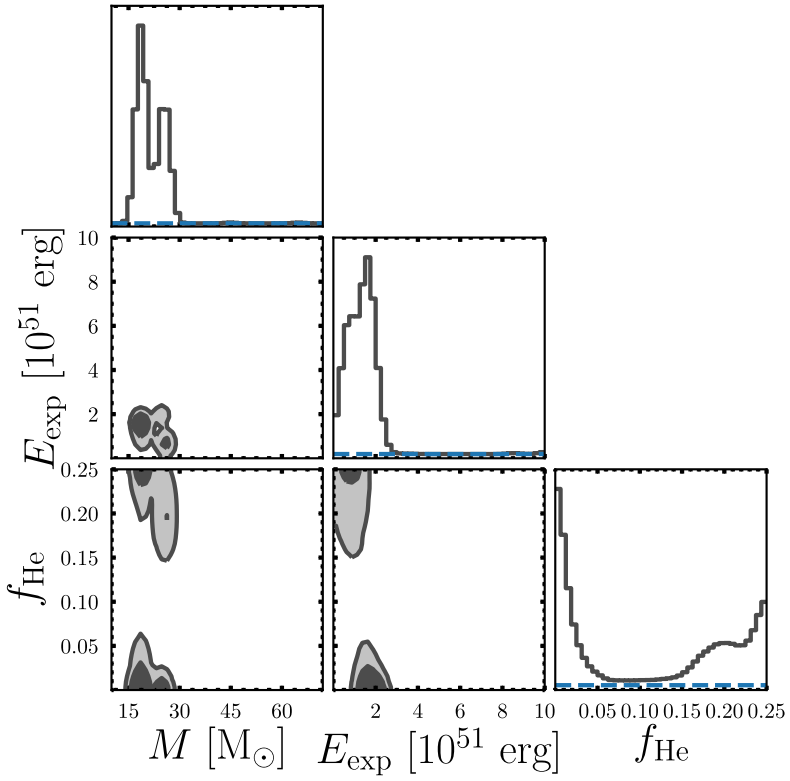

Figure 4. Results of our MCMC analysis of the chemical enrichment of the DLA towards J0903+2628 assuming the number of enriching stars $N_\star = 1$. From left to right, we show the progenitor star mass, the explosion energy, and the degree of mixing. The diagonal panels indicate the maximum likelihood posterior distributions of the model parameters while the 2D contours indicate the correlation between these parameters. The dark and light grey shaded regions indicate the 68 and 95 per cent confidence intervals, respectively. In the diagonal panels, the horizontal blue dashed line indicates the zero-level of each distribution.

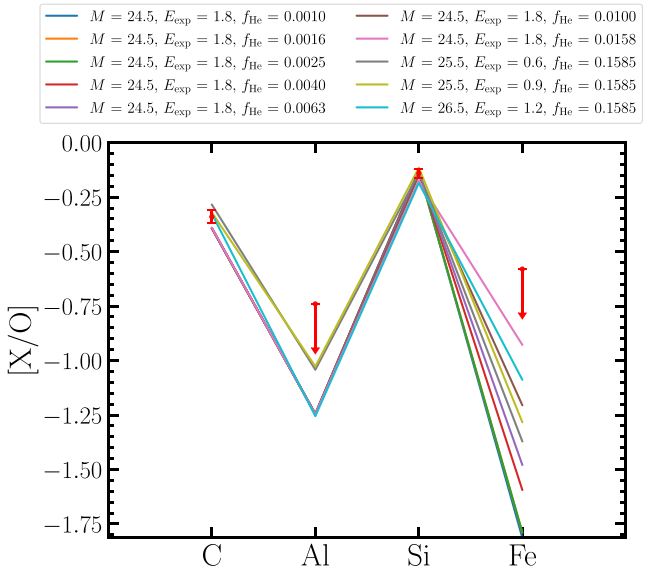

Figure 5. The predicted abundance patterns (coloured lines) for a selection of individual progenitor models that we have found are best able to model the data. The legend indicates the associated progenitor properties where M, $E_{\rm exp}$, and $f_{\rm He}$ are given in units of: $M_\odot$, 10^{51} erg, and fraction of the He core size. The observed abundances are shown as red symbols. Note the similarity in model parameters barring the degree of mixing. The range of the predicted [Fe/O] abundance is responsible for the large range shown in the right panel of Fig. 3.

modelled by the yields of an individual Population III SN rather than a small handful of these progenitors. Furthermore, given the best fitting models (i.e. those shown in Fig. 5), the predicted [C/Fe] abundance ratio suggest that this DLA may be in the UMP regime and could be significantly C-enhanced.

Another possibility is that Population II stars may have contributed some of the metals to this near-pristine DLA. The abundance ratios that are often accessible for the most metal-poor DLAs are [C/O], [Si/O], and [Fe/O]. The yields of these abundance ratios are broadly similar across both Population III and Population II stars (Welsh et al. 2019, fig. 1). This can make it challenging to disentangle the relative contributions of these populations based on yields alone. However, the tell-tale sign of enrichment from a primordial population of stars may be seen through empirical trends or, indeed, inferences of our model parameters – for example: a non-Salpeter IMF slope, a low number of enriching stars, or, an exotic explosion energy. Crucially, we do see this preference towards a low number of enriching stars in our analysis (Fig. 2 – top panel, second column). Further, if this were a Population II enriched system, we may expect the observed abundances to be consistent with the IMF-weighted abundances given a Salpeter IMF. This is not the case. Particularly, the IMF-weighted [O/Fe] abundance [O/Fe] $= +0.46$ (assuming a typical explosion energy and mixing; $E_{\rm exp} = 1.2 \times 10^{51}$ erg and $f_{\rm He} = 0.1$) is inconsistent with the observed lower limit provided by our new data. For completeness, we have also repeated our analysis under the assumption of enrichment by an individual Population II star and found that, using the yields from Woosley & Weaver (1995), the enrichment by a Population III star still provides the best fit to the data given the currently available yields (see Appendix B for further details).

The case of enrichment by an individual Population III SN is often reserved for the stellar relics found in the halo of the Milky Way and surrounding dwarf galaxies. In the following section, we discuss the implications of these results and draw comparisons with the chemistry of other relic objects. Ultimately, the goal is to reveal the nature of this most metal-poor DLA and its place within galaxy evolution.

5 DISCUSSION

The nature of DLAs, especially the most metal-poor systems is still an open question. Various interpretations have arisen since the first DLA survey. These highest H I column density absorption line systems could be associated with the discs of high redshift galaxies or, indeed, a wider range of galaxy masses and morphologies (Wolfe et al. 1986; Pettini, Boksenberg & Hunstead 1990; Haehnelt, Steinmetz & Rauch 1998). The latter scenario is supported by the results of both modern hydrodynamical cosmological simulations (e.g. Pontzen et al. 2008; Bird et al. 2013; Rahmati & Schaye 2014), and dedicated imaging surveys (e.g. Fumagalli et al. 2015). Searches for the emission from host galaxies aim to illuminate this issue. The use of integral field spectrographs have proven to be fruitful tools for these searches (e.g. Péroux et al. 2011, 2012; Fumagalli et al. 2017; Mackenzie et al. 2019; Berg et al. 2023; Lofthouse et al. 2023); as has the Atacama Large Millimeter/submillimeter Array (ALMA) (e.g. Møller et al. 2018; Neeleman et al. 2018; Klitsch et al. 2021). Surveys with these instruments may tentatively indicate that there is a more complicated relationship between the column density of the absorbing gas and its association with the host galaxy than initially thought (e.g. Lofthouse et al. 2023).

Specifically considering the environments of DLAs, the detection rate of associated galaxies has increased in recent years (e.g. Mackenzie et al. 2019; Klitsch et al. 2021). However, the presence of multiple galaxies (alongside their typically large impact parameters) in the observed fields make it challenging to assign a single host galaxy to the DLA. There are further complications related to the fraction of the DLA population associated with active star formation. It has been suggested that there may be a steep relationship between the emission luminosity of the host galaxy and the metallicity of the DLA (Krogager et al. 2017). The true nature of this relationship is an open question. If a mass–metallicity relation applies to galaxies at $z = 2$–3, the most metal-poor DLAs are likely to be associated with the faintest (and therefore most difficult to detect directly) host galaxies. Moreover, there is yet to be a detection in emission of a host galaxy associated with one of the four known EMP DLAs. Consequently, we look to other means to understand the association between the most metal-poor DLAs and galaxy evolution.

The chemistry of these environments is an invaluable tool to link these gaseous relics seen at high redshift to their local descendants. This is a necessary step to understand the role of near-pristine DLAs in galaxy evolution. Furthermore, it facilitates comparisons with other relic environments that may reveal similar enrichment histories and shared evolutionary pathways. For this reason, the following section is dedicated to comparing the chemistry of the most metal-poor DLA known to the stars within ultra-faint dwarf galaxies (UFDs).

5.1 Comparison with UFDs

We now compare the chemistry of this DLA to the chemistry of stars in the ultra faint dwarf galaxies (UFDs; $M_V > -7.7$ from the definition by Simon 2019) that orbit the Milky Way. The lowest mean metallicity of a confirmed UFD is that of Tucana II with [Fe/H] $= -2.9^{+0.15}_{-0.16}$ (Bechtol et al. 2015; Walker et al. 2016; Chiti et al. 2018; Simon 2019). These ancient galaxies are on the borderline of extreme metal-paucity and are considered relics of the early Universe (Bovill & Ricotti 2009; Muñoz et al. 2009; Salvadori & Ferrara 2009; Bromm & Yoshida 2011).

To fairly compare the metallicity of the DLA towards J0903+2628 with similar stellar relics would require the detection of the same elements in each system. Despite the wide range of element abundances available for stellar relics, there is relatively little chemical abundance overlap for the most metal-poor DLAs and stars. For the purpose of this work, we therefore reserve our analysis to comparing the relative abundance of a light atomic number element (in this case [C/H]) and an Fe-peak element, [Fe/H]. Fig. 6 shows [C/H] as a function of [Fe/H] for both metal-poor DLAs (grey squares) and stars within UFDs (colour-coded circles) as reported by the SAGA data base (Susa, Hasegawa & Tominaga 2014). We restrict our comparison to stars within UFDs with bounded [C/H] and [Fe/H] abundances. The EMP DLA reported here is shown as the red square. From this plot, we can see that the Fe-metallicity evolution of [C/H] reported for the most metal-poor DLAs is consistent with that of the stars within UFDs. We note that this may be influenced by the lack of known carbon-enhanced DLAs as well as potential observational biases due to the challenges of chemically characterizing the stars within the UFDs. The faint nature of these UFDs mean that we may only be observing, and subsequently characterizing, the brightest stars within these systems. This limitation will be drastically improved with the upcoming 4DWARFS survey (Skúladóttir et al. 2023).

Interestingly, there is an EMP star within Boötes I (large purple circle in Fig. 6) that occupies a similar parameter space as the DLA reported here. This star is known as Boo−1137. The relative abundances of mutual elements (i.e. those also detected towards J0903+2628) are provided in Table 2. These are taken from Norris et al. (2010) who used the solar scale log $\epsilon_{Fe} = 7.45$ (Asplund 2005).[8]

After rescaling the [Fe/H] abundance to the solar values adopted in this paper (see Table 1), Fig. 7 visualizes this comparison of similar relative abundances. While the upper limits provide limited information, the chemical make-ups of these two environments (the DLA and the star Boo−1137) appear to be consistent with each other. We speculate that this common chemical abundance pattern may indicate a common formation channel. In other words, the similar chemistry of these environments may imply they were enriched by a similar (possibly primordial) population of stars. We note that the [Mg/C], [Fe/H], and A(C) abundances of Boo−1137 are indicative of enrichment via Pop III SNe given the recent analysis by Rossi et al. (2023). We also point out that our comparison shows the chemical abundances relative to hydrogen. Consequently, the absolute abundances presented in Fig. 7 are dependent on the amount of hydrogen that the metals have mixed with. Under the assumption that at least *some* EMP stars form from EMP DLA gas, comparing the absolute abundances allows us to test how effectively the metals are mixed in EMP DLAs. The similar trends of EMP DLAs and stars seen in Fig. 7 supports our assumption, and the slight excess dispersion seen for the stellar sample could reflect intrinsic metallicity variations within EMP DLAs (i.e. EMP DLA gas is not entirely well-mixed) that

[8] log $\epsilon_X \equiv$ log (X/H) + 12. Note, we adopt the solar scale referenced in Table 1. In more recent stellar studies it is typical to assume log $\epsilon_{Fe} = 7.51$. This, like our solar scale, is drawn from Asplund et al. (2009). Though, we take the average solar Fe abundance reported from both photospheric and meteoritic determinations. On the solar scale typically used in stellar studies, our Fe limit would be [Fe/H] < -3.70 (2σ).

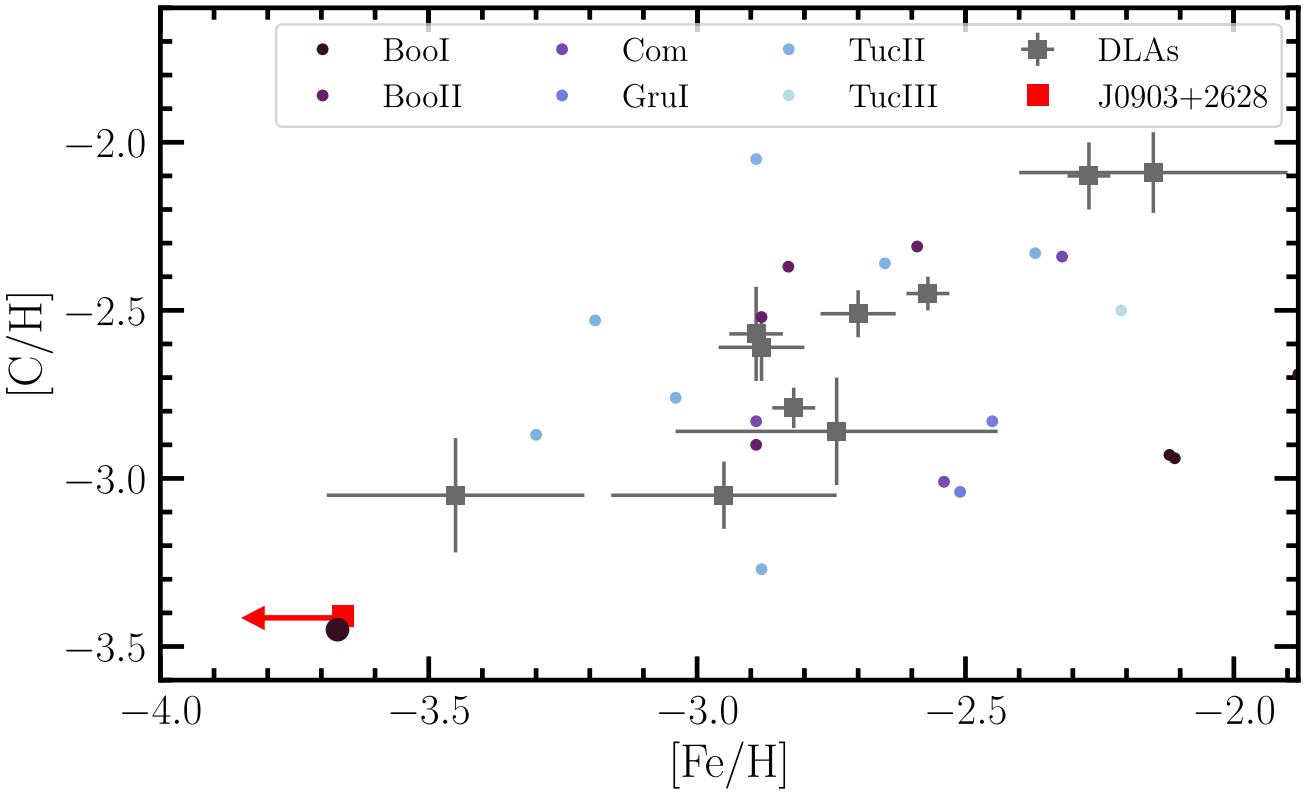

Figure 6. [C/H] versus [Fe/H] abundances of stars in ultra faint dwarf (UFD) galaxies alongside that of the most metal-poor DLAs. Stellar data are from the SAGA data base (Susa et al. 2014) and include the stars within these UFDs that have known [Fe/H] and [C/H] abundances with bounded errors. The stars from different systems are distinguished by their colour as described in the legend – sequentially: Boötes I, Boötes II, Coma Berenices, Grus I, Tucana II, Tucana III. The abundances of the DLA reported here are shown by the red square. For clarity, the circle of the star that occupies a similar parameter space to that of the DLA reported here (Boo−1137) has been enlarged.

Table 2. Elemental abundance ratios of Boo−1137 from Norris et al. (2010), corrected to the solar abundance scale adopted in our work. The quoted errors are the 1σ confidence limits while the upper limits are 2σ.

El	$[X/H]_{DLA}$	$[X/H]_{\star}$
C	-3.42 ± 0.06	-3.45 ± 0.20
O	-3.08 ± 0.05	<-1.75
Al	≤ -3.82	-4.35 ± 0.11
Si	-3.22 ± 0.05	-2.89 ± 0.16^{a}
Fe	≤ -3.66	-3.68 ± 0.11

Note. [a]This error is given by that of [Si/Fe] which is the ratio used in the MCMC enrichment model analysis.

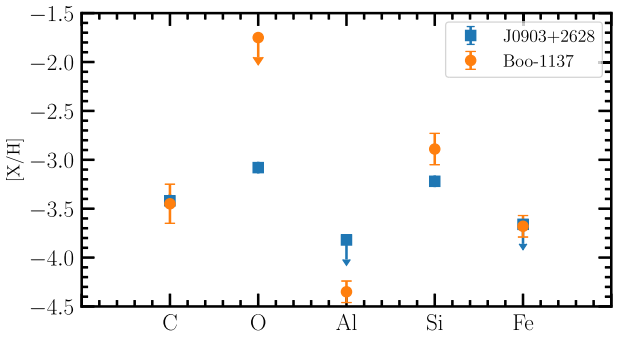

Figure 7. Comparisons of the [X/H] abundances of the chemical elements detected for both J0903+2628 (blue) and Boo−1137 (orange).

may reflect stochastic sampling of the IMF. Another possibility is that a single EMP DLA may comprise the gas and stars from chemically distinct minihaloes (e.g. Welsh, Cooke & Fumagalli 2021).

In order to understand the properties of the enriching population, we need to consider the relative abundances of *metals* (e.g. [C/Si] which is consistent for these objects). Repeating our MCMC analysis, under the assumption of enrichment from 1 Population III SN, the model for Boo−1137 converges on a progenitor mass that is remarkably similar to that found for J0903+2628. During this analysis, we utilized the same chemical elements used for J0903+2628. However, to accommodate the upper limit on [O/H], we consider the abundance ratios relative to Fe instead of O. The results of this analysis and the corresponding model fit to the data are shown in Figs 8 and 9, respectively.

Despite the broadly similar abundances and inferred progenitor mass, the inferred explosion energies differ; the stellar progenitor is well-modelled by a hypernova for Boo−1137 (i.e. $>5 \times 10^{51}$ erg) while the DLA progenitor is well-modelled by a more typical ($<3 \times 10^{51}$ erg) CCSN. A more striking agreement between the inferred progenitor properties is needed to provide a compelling argument for a singular enrichment channel. We are currently limited by the (lack of) information provided by the observed upper limits. Indeed, the [O/Fe] abundance limit of Boo−1137 is relatively weak ($[O/Fe]_{\star} <+1.9$) while that of J0903+2628 is not ($[O/Fe]_{DLA} >+0.58$). This is an important informant of the explosion energy (Heger & Woosley 2010; Limongi & Chieffi 2018, see also Appendix A). Furthermore, we could improve our

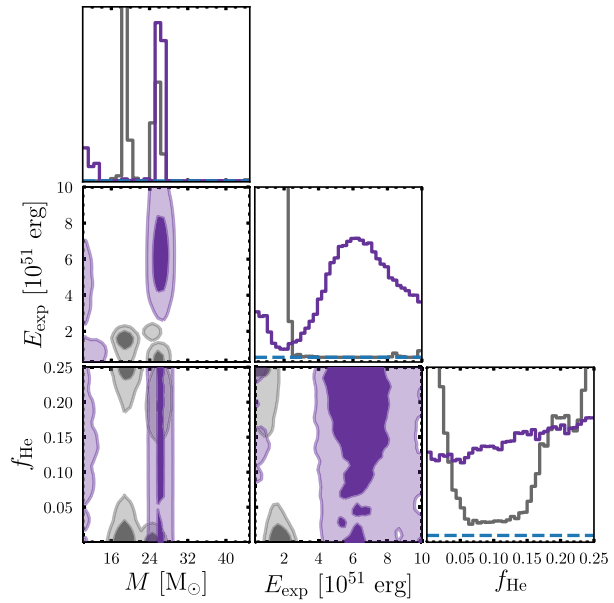

Figure 8. Same as Fig. 4, but based on the [C/Fe], [Si/Fe], [O/Fe], and [Al/Fe] of Boo−1137. The distributions associated with Boo−1137 are shown in purple while those for J0903+2628 (from Fig. 4) are shown in grey for reference.

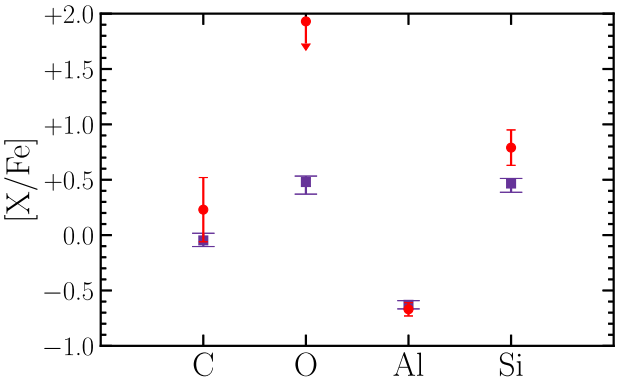

Figure 9. Same as Fig. 3, but based on the enrichment model inferred for Boo−1137 and colours match those in Fig. 8 (i.e. model results are shown in purple).

determination of the explosion energy by analysing the relative abundances of the Fe-peak elements of this DLA (Cooke et al. 2013). Using the AIC, we have checked which model is best able to reproduce the respective data of these objects. The model associated with the DLA data has a relatively lower AIC value (recall AIC = 3) than the model associated with the stellar data (AIC = 5). The relatively weaker performance of the Boo-1137 model can be seen in Fig. 9. This figure shows that the model is not able to reproduce the observed [Si/Fe] abundance within the 1σ errors when simultaneously reproducing the other abundance ratios.

As things stand, we need more data to link the most metal-poor DLA currently known to local analogues. This information can be gained in a multitude of ways. First, deeper NIR observations from the ground would allow the determination of the Fe column density through the Fe II λ2344 and Fe II λ2382 features (rather than the upper limit reported here). Furthermore, within the next decade, we will see the advent of the next generation of 30–40 m optical/IR ground-based telescopes, including the Extremely Large Telescope (ELT; Gilmozzi & Spyromilio 2007), the Giant Magellan Telescope (GMT; Johns et al. 2012), and the Thirty Meter Telescope (TMT; Skidmore, TMT International Science Development Teams & Science Advisory Committee 2015). With these facilities we will be able to study the *most* metal-poor DLAs with unprecedented sensitivity. Thus, we will be able to determine the abundances of elements whose features are too weak to efficiently observe with current facilities (e.g. the N, Mg, Al, S, Cr, Fe, Ni, and Zn abundances of J0903+2628). Beyond chemistry, we can use additional diagnostics (e.g. kinematics, density models, host galaxy emission, environment etc.) to investigate the properties of these ancient relics and their surrounding galaxy populations.

5.2 Observations with the JWST

With the *JWST*, it may be possible to detect light directly from the first stars at high redshift. However, depending on the adopted formation formalism, it may not be feasible to detect light from the first stellar population at $z > 8$ without the aide of lensing (Bovill et al. 2022); see also Trussler et al. (2022) for a more optimistic outlook.

The most metal-poor DLAs, and indeed near-pristine systems with lower column densities, provide a signpost to some of the least chemically polluted environments at $z_{\rm abs} < 6$. Such environments might be ideal to conduct searches for Population III stars at lower, more accessible, redshifts. Depending on the redshift of the absorber (e.g. $3 < z_{\rm abs} < 6$), the strong He II λ1640 Å feature expected from Population III stars may be most efficiently studied from the ground or from space (e.g. with HST/WFC3 or *JWST*/NIRCam). Once the strong He II λ1640 Å emission has been identified, *JWST*/NIRSpec is the optimal instrument to confirm the Population III nature of this emission by searching for strong H Balmer emission lines (indicative of an H II region), simultaneously combined with the absence of associated metal emission (e.g. [O III] λ 5007 Å).

We have performed an initial search for exotic stellar emission using the spectroscopic data presented here. Specifically, we search for any strong He II λ1640 Å emission at the redshift of the absorber (luminosity distance D_L = 26.8 Gpc) and do not detect anything. We model both the continuum and the potential feature using ALIS. The resulting 3σ upper limit on the flux density $f_\lambda < 8.5 \times 10^{-17}$ erg cm^{-2} s^{-1} Å^{-1} can be used to calculate the limit on the He II line luminosity after assuming an emission line width consistent with that found for local ($z < 0.01$) EMP galaxies (FWHM$_{\rm He}$ = 0.6 Å; Senchyna et al. 2019) and adopting the Planck Collaboration VI (2020) cosmology ($H_0 = 67.4 \pm 0.5$ kms^{-1}Mpc^{-1} and $\Omega_m = 0.315 \pm 0.007$). We place a conservative upper limit on the He II line luminosity of $<4.3 \times 10^{42}$ erg s^{-1} (3σ). This is over an order of magnitude above the predicted line luminosities from Schaerer (2003). Note that, this upper limit is only applicable to possible emission that is spatially coincident with the observed DLA. Without this proximity, we do not expect the stellar light to be covered by the slit used during these observations. To evaluate the possible star formation in the vicinity of this DLA, we would benefit from additional information beyond an individual sightline.

Given the challenges associated with detecting Population III stars at $z > 8$, the most metal-poor DLAs may be invaluable tools in the search for light from the first stars. Over the coming years, observational surveys are necessary to explore how efficient these DLAs are as beacons for the first stars and galaxies, and more generally, to study the most metal barren environments in the Universe. Furthermore, the firm detection of a Population III stellar signature associated with these DLA host galaxies would confirm the relic nature of these environments.

6 CONCLUSIONS

We present the updated chemical abundances of the DLA towards J0903+2628 based on data collected with Keck I/HIRES. These data reaffirm that this gas reservoir is the most metal-poor DLA currently known. Our main conclusions are as follows:

(i) The latest data provide an upper limit on the iron abundance, [Fe/H]≤ -3.66 (2σ). This is a 0.85 dex improvement on the previous upper limit and confirms that this DLA is indeed EMP, and could possibly be the first UMP DLA. To secure the first firm detection of Fe in this system will require further observations. This would require a significant time investment on 8–10 m class telescopes. Alternatively, the required sensitivity will be efficiently achieved with the next generation of 30–40 m telescopes.

(ii) The current data indicate that *all* of the detected α-elements (C, O, and Si) are enhanced relative to iron, compared to a typical very metal-poor DLA. We speculate that this intriguing gas cloud may have an iron abundance considerably below the current detection limit. Such an Fe-deficient abundance pattern is reminiscent of the α-enhanced (or, rather, Fe-deficient) stars in the halo of the Milky Way.

(iii) We apply a stochastic chemical enrichment model to investigate the properties of the stars that have enriched this gaseous relic. The results of this analysis suggest that the chemistry of this environment is best modelled by a low number of enriching stars. The observed abundance pattern is well-modelled by an individual Population III SN with an initial progenitor mass $M = (18–27)\mathrm{M}_{\odot}$ (2σ).

(iv) We compare the chemistry of this DLA to the abundances of the most metal-poor stars in the UFDs orbiting the Milky Way. The star closest in chemistry to that of the DLA towards J0903+2628 is Boo−1137 in Boötes I with [Fe/H] $= -3.68 \pm 0.11$ (registered onto our adopted solar scale; Norris et al. 2010). The [X/H] abundances that are measured in both relics are broadly consistent (though we are often restricted to upper limits). This may indicate that Boo−1137 formed from gas that was enriched through a similar mechanism to that of J0903+2628. Indeed, our analysis tentatively supports the scenario in which these relics have been enriched by a single Population III progenitor with similar mass properties but with notably distinct explosion properties.

Our work highlights that, while rare, near-pristine DLAs are an invaluable probe of the metals produced by some of the earliest stars in the Universe. These gaseous relics may also provide a signpost to some of the least polluted environments of the Universe and thus act as beacons to search for light from the first stars directly using the *JWST*.

ACKNOWLEDGEMENTS

We thank the referee for a constructive report that improved the presentation of this work. We thank Rajeshwari Dutta and both the organisers and participants of the first stars IFPU focus week (2023 May 15–19) for helpful discussions. This paper is based on observations collected at the W. M. Keck Observatory which is operated as a scientific partnership among the California Institute of Technology, the University of California and the National Aeronautics and Space Administration. The Observatory was made possible by the generous financial support of the W. M. Keck Foundation. The authors wish to recognize and acknowledge the very significant cultural role and reverence that the summit of Maunakea has always had within the indigenous Hawaiian community. We are most fortunate to have the opportunity to conduct observations from this mountain. We are also grateful to the staff astronomers at Keck Observatory for their assistance with the observations.

This work has been supported by Fondazione Cariplo, grant No 2018–2329. During this work, RJC was supported by a Royal Society University Research Fellowship. We acknowledge support from the Science and Technology Facilities Council (STFC) (ST/T000244/1). This project has received funding from the European Research Council (ERC) under the European Union's Horizon 2020 research and innovation programme (grant agreement No 757535). This work used the DiRAC@Durham facility managed by the Institute for Computational Cosmology on behalf of the STFC DiRAC HPC Facility (www.dirac.ac.uk). The equipment was funded by BEIS capital funding via STFC capital grants ST/K00042X/1, ST/P002293/1, ST/R002371/1, and ST/S002502/1, Durham University, and STFC operations grant ST/R000832/1. DiRAC is part of the National e-Infrastructure. This research has made use of NASA's Astrophysics Data System.

Facilities: Keck: I (HIRES)

Software: ASTROPY (Astropy Collaboration 2013), CORNER (Foreman-Mackey 2016), EMCEE (Foreman-Mackey et al. 2013), MATPLOTLIB (Hunter 2007), and NUMPY (van der Walt, Colbert & Varoquaux 2011).

DATA AVAILABILITY

The data underlying this article are available through the Keck Observatory Archive. The processed data used by the authors is available via request.

REFERENCES

Abel T., Bryan G. L., Norman M. L., 2002, Science, 295, 93
Akaike H., 1974, IEEE Trans. Autom. Control, 19, 716
Akerman C. J., Ellison S. L., Pettini M., Steidel C. C., 2005, A&A, 440, 499
Asplund M., 2005, ARA&A, 43, 481
Asplund M., Grevesse N., Sauval A. J., Scott P., 2009, ARA&A, 47, 481
Astropy Collaboration 2013, A&A, 558, A33
Bañados E. et al., 2019, ApJ, 885, 59
Barkana R., Loeb A., 2001, Phys. Rep., 349, 125
Bechtol K. et al., 2015, ApJ, 807, 50
Becker G. D., Sargent W. L. W., Rauch M., Calverley A. P., 2011, ApJ, 735, 93
Becker G. D. et al., 2019, ApJ, 883, 163
Beers T. C., Carollo D., 2008, in O'Shea B. W., Heger A., eds, AIP Conf. Proc. Vol. 1170, Stellar 990, First Stars III. Am. Inst. Phys., New York, p. 104
Beers T. C., Christlieb N., 2005, ARA&A, 43, 531
Beers T. C., Preston G. W., Shectman S. A., 1985, AJ, 90, 2089
Beers T. C., Preston G. W., Shectman S. A., 1992, AJ, 103, 1987
Berg M. A. et al., 2023, ApJ, 944, 101
Bernstein R. M., Burles S. M., Prochaska J. X., 2015, PASP, 127, 911
Bird S., Vogelsberger M., Sijacki D., Zaldarriaga M., Springel V., Hernquist L., 2013, MNRAS, 429, 3341
Bond H. E., 1980, ApJS, 44, 517
Bosman S. E. I., Becker G. D., 2015, MNRAS, 452, 1105
Bosman S. E. I. et al., 2022, MNRAS, 514, 55
Bovill M. S., Ricotti M., 2009, ApJ, 693, 1859
Bovill M. S., Stiavelli M., Wiggins A. I., Ricotti M., Trenti M., 2022, preprint (arXiv:2210.10190)
Bromm V., Yoshida N., 2011, ARA&A, 49, 373
Bromm V., Coppi P. S., Larson R. B., 2002, ApJ, 564, 23
Cayrel R. et al., 2004, A&A, 416, 1117
Chiti A., Frebel A., Ji A. P., Jerjen H., Kim D., Norris J. E., 2018, ApJ, 857, 74

Christlieb N., Schörck T., Frebel A., Beers T. C., Wisotzki L., Reimers D., 2008, A&A, 484, 721
Clark P. C., Glover S. C. O., Klessen R. S., Bromm V., 2011, ApJ, 727, 110
Cooke R., Pettini M., Steidel C. C., Rudie G. C., Jorgenson R. A., 2011a, MNRAS, 412, 1047
Cooke R., Pettini M., Steidel C. C., Rudie G. C., Nissen P. E., 2011b, MNRAS, 417, 1534
Cooke R., Pettini M., Jorgenson R. A., Murphy M. T., Rudie G. C., Steidel C. C., 2013, MNRAS, 431, 1625
Cooke R. J., Pettini M., Jorgenson R. A., 2015, ApJ, 800, 12
Cooke R. J., Pettini M., Nollett K. M., Jorgenson R., 2016, ApJ, 830, 148
Cooke R. J., Pettini M., Steidel C. C., 2017, MNRAS, 467, 802 (C17)
de Jong R. S. et al., 2012, in McLean I. S., Ramsay S. K., Takami H., eds, Proc. SPIE Conf. Ser. Vol. 8446, Ground-based and Airborne Instrumentation for Astronomy IV. SPIE, Bellingham, p. 84460T
DESI Collaboration 2016, preprint (arXiv:1611.00036)
D'Odorico V. et al., 2022, MNRAS, 512, 2389
D'Odorico V. et al., 2023, MNRAS, 523, 1399
Dalton G. et al., 2012, in McLean I. S., Ramsay S. K., Takami H., eds, Proc. SPIE Conf. Ser. Vol. 8446, Ground-based and Airborne Instrumentation for Astronomy IV. SPIE, Bellingham, p. 84460P
Dutta R., Srianand R., Rahmani H., Petitjean P., Noterdaeme P., Ledoux C., 2014, MNRAS, 440, 307
Ellison S. L., Prochaska J. X., Hennawi J., Lopez S., Usher C., Wolfe A. M., Russell D. M., Benn C. R., 2010, MNRAS, 406, 1435
Erni P., Richter P., Ledoux C., Petitjean P., 2006, A&A, 451, 19
Foreman-Mackey D., 2016, J. Open Source Softw., 1, 24
Foreman-Mackey D., Hogg D. W., Lang D., Goodman J., 2013, PASP, 125, 306
Fumagalli M., O'Meara J. M., Prochaska J. X., 2011, Science, 334, 1245
Fumagalli M., O'Meara J. M., Prochaska J. X., Rafelski M., Kanekar N., 2015, MNRAS, 446, 3178
Fumagalli M. et al., 2017, MNRAS, 471, 3686
Gardner J. P. et al., 2009, in Thronson H. A., Stiavelli M., Tielens A., eds, Astrophysics in the Next Decade. Springer, Dordrecht, p. 1
Gilmozzi R., Spyromilio J., 2007, The Messenger, 127, 11
Greif T. H., Glover S. C. O., Bromm V., Klessen R. S., 2010, ApJ, 716, 510
Haehnelt M. G., Steinmetz M., Rauch M., 1998, ApJ, 495, 647
Heger A., Woosley S. E., 2010, ApJ, 724, 341 (HW10)
Hirano S., Hosokawa T., Yoshida N., Umeda H., Omukai K., Chiaki G., Yorke H. W., 2014, ApJ, 781, 60
Howes L. M. et al., 2016, MNRAS, 460, 884
Hunter J. D., 2007, Comput. Sci. Eng., 9, 90
Johns M. et al., 2012, in Stepp L. M., Gilmozzi R., Hall H. J., eds, Proc. SPIE Conf. Ser. Vol. 8444, Ground-based and Airborne Telescopes IV. SPIE, Bellingham, p. 84441H
Klitsch A., Péroux C., Zwaan M. A., De Cia A., Ledoux C., Lopez S., 2021, MNRAS, 506, 514
Krogager J. K., Møller P., Fynbo J. P. U., Noterdaeme P., 2017, MNRAS, 469, 2959
Limongi M., Chieffi A., 2018, ApJS, 237, 13
Lodders K., 2019, preprint (arXiv:1912.00844)
Lofthouse E. K. et al., 2023, MNRAS, 518, 305
Mackenzie R. et al., 2019, MNRAS, 487, 5070
McWilliam A., Preston G. W., Sneden C., Shectman S., 1995, AJ, 109, 2736
Møller P. et al., 2018, MNRAS, 474, 4039
Muñoz J. A., Madau P., Loeb A., Diemand J., 2009, MNRAS, 400, 1593
Neeleman M., Kanekar N., Prochaska J. X., Christensen L., Dessauges-Zavadsky M., Fynbo J. P. U., Møller P., Zwaan M. A., 2018, ApJ, 856, L12
Norris J. E., Yong D., Gilmore G., Wyse R. F. G., 2010, ApJ, 711, 350
Noterdaeme P. et al., 2021, A&A, 651, A78
Nuñez E. H., Kirby E. N., Steidel C. C., 2022, ApJ, 927, 64
Péroux C., Howk J. C., 2020, ARA&A, 58, 363
Péroux C., Bouché N., Kulkarni V. P., York D. G., Vladilo G., 2011, MNRAS, 410, 2251
Péroux C., Bouché N., Kulkarni V. P., York D. G., Vladilo G., 2012, MNRAS, 419, 3060
Pettini M., Boksenberg A., Hunstead R. W., 1990, ApJ, 348, 48
Pettini M., King D. L., Smith L. J., Hunstead R. W., 1997, ApJ, 478, 536
Pettini M., Zych B. J., Steidel C. C., Chaffee F. H., 2008, MNRAS, 385, 2011
Pieri M. M. et al., 2016, in Reylé C., Richard J., Cambrésy L., Deleuil M., Pécontal E., Tresse L., Vauglin I., eds, SF2A-2016: Proceedings of the Annual meeting of the French Society of Astronomy and Astrophysics. French Society of Astronomy and Astrophysics, Lyon, France, p. 259
Planck Collaboration VI, 2020, A&A, 641, A6
Pontzen A. et al., 2008, MNRAS, 390, 1349
Rafelski M., Wolfe A. M., Prochaska J. X., Neeleman M., Mendez A. J., 2012, ApJ, 755, 89
Rafelski M., Neeleman M., Fumagalli M., Wolfe A. M., Prochaska J. X., 2014, ApJ, 782, L29
Rahmati A., Schaye J., 2014, MNRAS, 438, 529
Robert P. F., Murphy M. T., O'Meara J. M., Crighton N. H. M., Fumagalli M., 2019, MNRAS, 483, 2736
Roederer I. U., Preston G. W., Thompson I. B., Shectman S. A., Sneden C., Burley G. S., Kelson D. D., 2014, AJ, 147, 136
Rossi M., Salvadori S., Skúladóttir Á., Vanni I., 2023, MNRAS, 533, L1
Ryan S. G., Norris J. E., Bessell M. S., 1991, AJ, 102, 303
Ryan S. G., Norris J. E., Beers T. C., 1996, ApJ, 471, 254
Saccardi A. et al., 2023, ApJ, 948, 35
Salvadori S., Ferrara A., 2009, MNRAS, 395, L6
Schaerer D., 2003, A&A, 397, 527
Senchyna P., Stark D. P., Chevallard J., Charlot S., Jones T., Vidal-García A., 2019, MNRAS, 488, 3492
Simcoe R. A., Sullivan P. W., Cooksey K. L., Kao M. M., Matejek M. S., Burgasser A. J., 2012, Nature, 492, 79
Simon J. D., 2019, ARA&A, 57, 375
Skidmore W., Science Advisory Committee T., TMT International Science Development Teams, , 2015, Res. Astron. Astrophys., 15, 1945
Skúladóttir Á. et al., 2023, The Messenger, 190, 19
Stacy A., Bromm V., Lee A. T., 2016, MNRAS, 462, 1307
Starkenburg E. et al., 2017, MNRAS, 471, 2587
Sukhbold T., Woosley S. E., Heger A., 2018, ApJ, 860, 93
Susa H., Hasegawa K., Tominaga N., 2014, ApJ, 792, 32
Tegmark M., Silk J., Rees M. J., Blanchard A., Abel T., Palla F., 1997, ApJ, 474, 1
Trussler J. A. A., Conselice C. J., Adams N. J., Maiolino R., Nakajima K., Zackrisson E., Ferreira L., 2022, preprint (arXiv:2211.02038)
Turk M. J., Abel T., O'Shea B., 2009, Science, 325, 601
van der Walt S., Colbert S. C., Varoquaux G., 2011, Comput. Sci. Eng., 13, 22
Vladilo G., Abate C., Yin J., Cescutti G., Matteucci F., 2011, A&A, 530, A33
Vogt S. S. et al., 1994, in Crawford D. L., Craine E. R., eds, Proc. SPIE Conf. Ser. Vol. 2198, Instrumentation in Astronomy VIII. SPIE, Bellingham, p. 362
Walker M. G. et al., 2016, ApJ, 819, 53
Welsh L., Cooke R., Fumagalli M., 2019, MNRAS, 487, 3363
Welsh L., Cooke R., Fumagalli M., Pettini M., 2020, MNRAS, 494, 1411
Welsh L., Cooke R., Fumagalli M., 2021, MNRAS, 500, 5214
Welsh L., Cooke R., Fumagalli M., Pettini M., 2022, ApJ, 929, 158
Wolfe A. M., Turnshek D. A., Smith H. E., Cohen R. D., 1986, ApJs, 61, 249
Wolfe A. M., Gawiser E., Prochaska J. X., 2005, ARA&A, 43, 861
Woosley S. E., 2017, ApJ, 836, 244
Woosley S. E., Weaver T. A., 1995, ApJS, 101, 181
Zou S., Petitjean P., Noterdaeme P., Ledoux C., Srianand R., Jiang L., Krogager J.-K., 2020, ApJ, 901, 105

APPENDIX A: COMPARISON WITH COOKE ET AL. (2017)

In this appendix, we compare the results of our MCMC model analysis to that determined using the original data reported in Cooke et al. (2017) (hereafter C17). Specifically, we compare the inferred properties of an individual Pop III progenitor that may have enriched this gas cloud. The data presented in C17 facilitated the high-

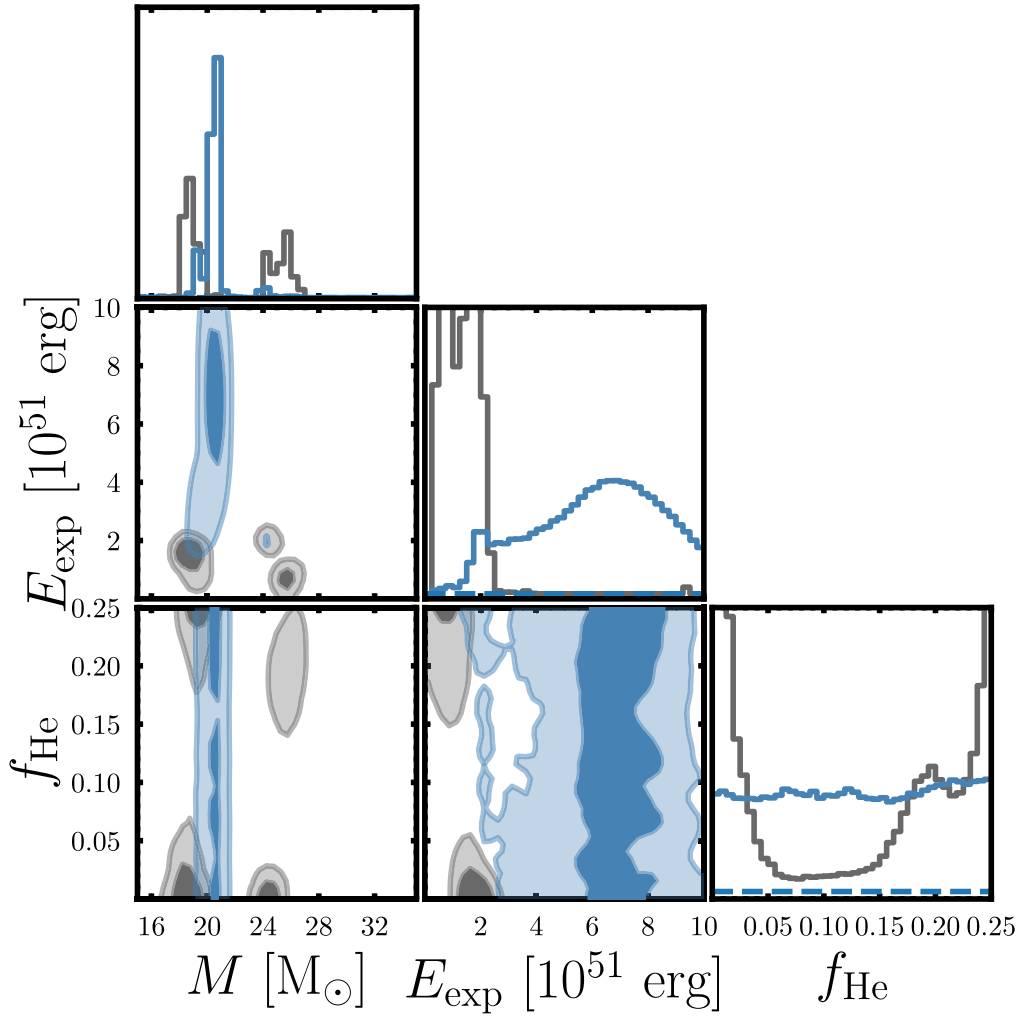

Figure A1. Same as Fig. 4 (grey contours) overplotted with the parameter distributions presented in C17 (blue contours).

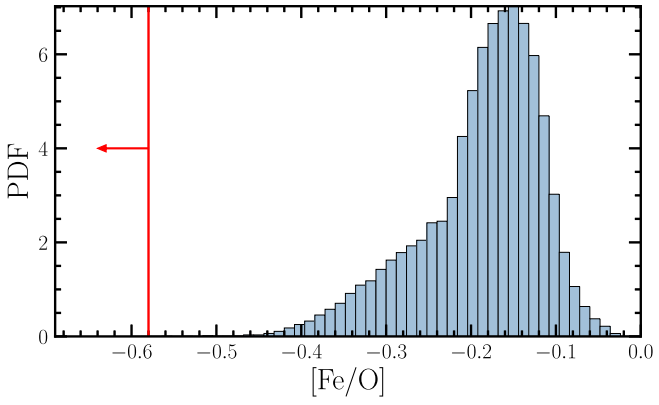

Figure A2. The predicted distribution of [Fe/O] (blue histogram) based on the model parameters inferred from the C17 analysis of J0903+2628 compared to the limit given the latest observational data (red line and arrow).

precision determination of both the [C/O] and [Si/O] abundances of J0903+2628: [C/O] $=-0.38 \pm 0.03$ and [Si/O] $=-0.16 \pm 0.02$. These data also provided the first limit on the [Fe/O] abundance ratio: [Fe/O] $<+0.23$. Given that the typical [Fe/O] abundance of very metal-poor DLAs (i.e. $-3 <$ [Fe/H] < -2) is [Fe/O] ~-0.40, this limit is not particularly informative (Cooke et al. 2011a; Welsh et al. 2022). As discussed in the introduction, the original analysis was constrained by the original wavelength coverage of the data. The data presented in this work allow us to improve the constraint on [O/Fe] by $\sim$1 dex and further provide the abundance limit of an additional element [Al/O]. As such, it is illuminating to explore how the information contained in these additional abundance ratio determinations inform our inferred enrichment model parameters; this comparison is shown in Fig. A1. The grey contours are identical to those presented in Fig. 4 while the blue contours correspond to those presented in fig. 3 of C17. Note that the MCMC modelling procedure adopted for both models is consistent. Explicitly, the abundance ratios used to inform the blue contours are [C/O] and [Si/O]. These are also used to inform the grey contours with the additional lower limits placed on [Fe/O] and [Al/O].

Analysing the full complement of data, alongside a technique that utilizes abundance ratios with lower limits, we infer different model parameters to those of C17. The inferred progenitor masses are not too dissimilar. The most notable distinction is the preference towards low explosion energies when using the latest data and the preference towards a hypernova when exclusively considering the C17 data. Fig. A2 may explain a driving force behind this difference. This figure showcases the expected distribution of [Fe/O] based on the Pop III progenitor properties inferred by C17 alongside the

limit based on the observational data reported here. From this, it is clear that the observed limit on [Fe/O] is not reproducible given the C17 progenitor properties. As mentioned in Section 5, [Fe/O] is an important informant of an enriching progenitor's explosion properties. Indeed, this can be seen by the marked improvement on the constraints of $E_{\rm exp}$.

Ultimately, this comparison highlights that these new data provide critical information on the heavy elements and odd-atomic number elements present in this gas cloud that allow us to better study the potential enrichment history of this most metal-poor DLA. The latest model represents the progenitor properties best able to reproduce the current data. The power of our enrichment model analysis comes from simultaneously reproducing the observed abundances of relic objects. As this comparison highlights, these progenitor properties are influenced by the available abundance ratios and much can be inferred from a few key additional elements. As such, it is exciting to think what will be achieved with the next generation of ground-based telescopes (e.g. ELT/ANDES) and the detection of elements like Cr, Ni, and Zn.

APPENDIX B: ENRICHMENT BY POPULATION II STARS

In this appendix, we repeat our MCMC analysis to find the properties of 1 Population II SN that best match the abundances of the DLA reported here. For this analysis we utilize a subset of the yields from Woosley & Weaver (1995) whose progenitor metallicities are $Z = 0.0001 Z_{\odot}$. These yields span a mass range of $M = (12–40)\ {\rm M}_{\odot}$; this is the same region explored during our analysis. The yields are calculated using a fixed explosion energy and mixing parameter; therefore the only free parameter in this analysis is the progenitor mass. We find the yields are best modelled by a star will a mass of $M \sim 27\,{\rm M}_{\odot}$. The relative abundances estimated given the inferred Population II properties (orange symbols) are shown in Fig. B1 alongside the observed abundances (red symbols) and those calculated from our analysis using Population III yields (grey symbols). From this figure, we can see that the Population III yields are a better fit to the data than that provided by the Population II yields. A caveat to note is that the Population II yields are comparatively limited given the fixed explosion energy and mixing parameter adopted during the Woosley & Weaver (1995) simulations. It would be interesting to see whether Population II yields that explore a similar parameter space as the HW10 yields could produce a better fitting model. However, given the publicly available yields, we conclude that a Population III progenitor is best able to replicate the observed relative abundances.

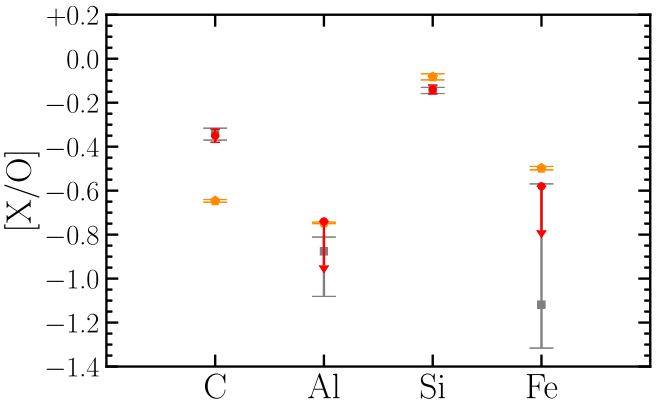

Figure B1. Same as Fig. 3, but shows the enrichment model inferred for a Population II progenitor (orange) alongside those inferred for a Population III progenitor (grey). The red symbols indicate the current observationally measured abundances.

This paper has been typeset from a TEX/LATEX file prepared by the author.